J. Fluid Mech. (1985), *vol.* 150, *pp.* 121–138
Printed in Great Britain

Fluid motion inside a spinning nutating cylinder

By HAROLD R. VAUGHN, WILLIAM L. OBERKAMPF AND WALTER P. WOLFE

Aeroballistics Division 1631, Sandia National Laboratories, Albuquerque, New Mexico 87185

(Received 21 February 1984)

The incompressible three-dimensional Navier–Stokes equations are solved numerically for a fluid-filled cylindrical cannister that is spinning and nutating. The motion of the cannister is characteristic of that experienced by spin-stabilized artillery projectiles. Equations for the internal fluid motion are derived in a non-inertial aeroballistic coordinate system. Steady-state numerical solutions are obtained by an iterative finite-difference procedure. Flow fields and liquid induced moments have been calculated for viscosities in the range of 0.9×10^4–1×10^9 cSt. The nature of the three-dimensional fluid motion inside the cylinder is discussed, and the moments generated by the fluid are explained. The calculated moments generally agree with experimental measurements.

1. Introduction

Flight instabilities of artillery projectiles due to certain liquid fills have been documented in recent years by D'Amico (1978), Miller (1982), and others. D'Amico & Miller (1979) flight-tested shells with similar liquid payloads ranging in viscosity from 10^3 to 1.7×10^5 cSt. Miller (1982) measured the liquid-induced despin moment with a laboratory fixture capable of both spinning and nutating a cylindrical canister filled with homogenous liquids ranging in viscosity from 1 cSt to 2×10^6 cSt. The existence of a large despin moment and nutational instability produced by the viscous liquids was clearly demonstrated by the laboratory and flight tests. The immediate problem was solved (Miller 1979; D'Amico 1981) by packing the payload section with circular felt wedges which were impregnated with the liquid payload (phosphorus). These wedges had the effect of severely restricting the motion of the fluid. However, the cause of the problem remained obscure, because the internal fluid motion is extremely difficult to experimentally measure and to analyse. An early attempt by Vaughn (1978) to derive the parametric dependence of the moments involved excessive physical assumptions and provided little physical insight. Murphy (1982) obtained a theoretical solution for the pitch and yaw moment with an improved version of the Stewartson (1958)–Wedemeyer (1966) theory at the lower viscosities. Recent work by Murphy (1983) derives a relation between the liquid-induced roll moment and the side moment. Unfortunately, the Stewartson approach does not seem to produce the required roll torque, and both efforts seem to be limited to the lower-viscosity range.

Since none of the previous references provide an understanding of the motion of the fluid in the high-viscosity range, where the destabilizing moments are the largest, it was decided to solve the Navier–Stokes equations numerically for a spinning nutating fluid-filled cylinder. Equations for the internal fluid motion were derived in a non-inertial aeroballistic coordinate system. The three-dimensional internal flow field was solved for a viscosity range of 0.9×10^4–1×10^9 cSt using an iterative

finite-difference method. The results show that the flow is fully three-dimensional, as might be expected, and dominated by viscous effects. The calculated moments generally agree with experimental roll and yaw moments.

2. Derivation of equations

2.1. *Non-inertial coordinate system*

A numerical solution to the fluid motion inside a spinning and nutating cylinder requires that careful consideration be given to the choice of the coordinate system. The two primary candidates are the body-fixed and the aeroballistic coordinate systems. In the body-fixed coordinate system the axes are attached to the cylinder, and therefore spin and nutate with the cylinder. In the present aeroballistic system the axes nutate with the cylinder, but they do not spin.

The criterion for the selection of the appropriate coordinate system must be the nature of the boundary conditions and solution in each system. Experiments by Miller (1981) have revealed some fundamental features of the flow field. Miller has taken high-speed motion pictures of a partially filled circular cylinder that is spinning and nutating at constant rates. For the artillery-shell case, when the spin frequency is much greater than the nutational frequency, the photographs show a void near the axis of the cylinder. For high-viscosity fluids, the shape of the void is a cylinder with a slightly S-curved axis, which appears to be constant in shape and orientation with respect to the nutation axis. For low-viscosity fluids the cylindrical void becomes more distorted, and small-scale disturbances are seen on the air/fluid interface. These experiments support the view that for high-viscosity fluids the flow field is steady, i.e. non-time-varying, in the aeroballistic reference frame. The flow field in the body-fixed system would therefore be time-varying and periodic, with a period of $2\pi/\omega_s$, where ω_s is the spin rate measured in the aeroballistic reference frame. A considerably greater numerical effort would be required to obtain the solution in the body-fixed system. Consequently, in the present analysis the equations of motion are derived in an aeroballistic reference frame.

In their traditional development (Schlichting 1968) the Navier–Stokes equations are derived in an inertial coordinate system. The aeroballistic coordinate system is, by virtue of its nutation, a non-inertial coordinate system. The Navier–Stokes equations must therefore be rederived taking into account the appropriate acceleration terms for the nutating axes.

2.2. *Fluid-flow equations*

The Navier–Stokes equations are to be derived in a non-inertial, non-spinning, nutating, aeroballistic axis system (figure 1). It should be noted that standard aeroballistic axes in flight dynamics do not spin or nutate. The present aeroballistic axes have a rotation rate, relative to inertial space, equal to the nutation rate. The incompressible Navier–Stokes equations for an inertial frame of reference can be written as

$$\frac{\mathrm{D}\boldsymbol{V}}{\mathrm{D}t} = \frac{\boldsymbol{F}}{\rho} - \frac{1}{\rho}\boldsymbol{\nabla} p + \nu \nabla^2 \boldsymbol{V}, \tag{1}$$

where $\boldsymbol{V} \equiv$ the absolute velocity of a fluid particle, $\boldsymbol{F} \equiv$ the body force, e.g. gravity, $\rho \equiv$ fluid density, $p \equiv$ static pressure and $\nu \equiv$ kinematic viscosity.

To be applied in a non-inertial reference frame, both the acceleration vector appearing in the left-hand side of (1) and the velocity vector appearing in the viscosity term must be expanded to account for the rotation of the axes.

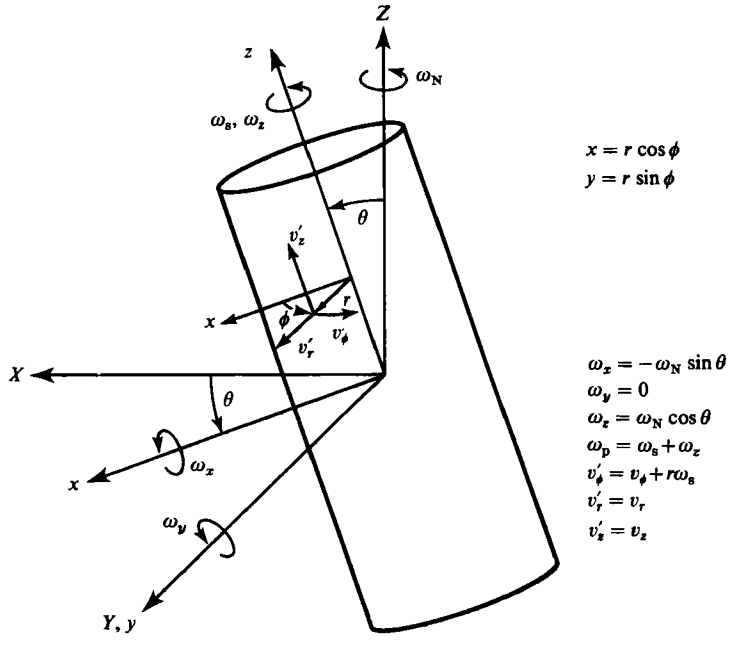

FIGURE 1. Axis system.

The velocity vector $\boldsymbol{V}$ may be written as

$$\boldsymbol{V} = \boldsymbol{V}' + \boldsymbol{\Omega} \times \boldsymbol{R} + \boldsymbol{V}_c, \tag{2}$$

where $\boldsymbol{V}' \equiv$ velocity relative to the aeroballistic axis system, $\boldsymbol{\Omega} \equiv$ rotation vector of the axes, $\boldsymbol{R} \equiv$ position vector relative to the aeroballistic system, and $\boldsymbol{V}_c \equiv$ linear velocity of the coordinate system. By performing the vector operations, it can be shown that

$$\nabla^2(\boldsymbol{\Omega} \times \boldsymbol{R}) = 0. \tag{3}$$

Also, for this application it is assumed that

$$\boldsymbol{V}_c = 0. \tag{4}$$

The right-hand side of (1) is therefore unaffected by the axes' rotation.

Any absolute acceleration may be written in a non-inertial reference frame as (Meriam 1975; Raudkivi & Callander 1975)

$$\boldsymbol{A} = \boldsymbol{A}_c + \boldsymbol{A}' + 2\boldsymbol{\Omega} \times \boldsymbol{V}' + \boldsymbol{\Omega} \times (\boldsymbol{\Omega} \times \boldsymbol{R}) + \dot{\boldsymbol{\Omega}} \times \boldsymbol{R} \tag{5}$$

where $\boldsymbol{A}_c \equiv$ linear acceleration of coordinate system and $\boldsymbol{A}' = \mathrm{D}\boldsymbol{V}'/\mathrm{D}t \equiv$ fluid acceleration relative to the aeroballistic axes. For the case considered here it is assumed that

$$\boldsymbol{A}_c = 0 \tag{6}$$

and that the axes are rotating at a constant speed,

$$\dot{\boldsymbol{\Omega}} = 0. \tag{7}$$

Substituting (2)–(7) into (1) gives

$$\frac{\mathrm{D}\boldsymbol{V}'}{\mathrm{D}t} + 2\boldsymbol{\Omega} \times \boldsymbol{V} + \boldsymbol{\Omega} \times (\boldsymbol{\Omega} \times \boldsymbol{R}) = \frac{\boldsymbol{F}}{\rho} - \frac{1}{\rho}\nabla p + \nu\nabla^2 \boldsymbol{V}'. \tag{8}$$

Since
$$\frac{\mathrm{D}\boldsymbol{V}'}{\mathrm{D}t} = \frac{\partial \boldsymbol{V}'}{\partial t} + (\boldsymbol{V}' \cdot \boldsymbol{\nabla})\, \boldsymbol{V}', \tag{9}$$

(8) may be written as

$$\frac{\partial \boldsymbol{V}'}{\partial t} = -(\boldsymbol{V}' \cdot \boldsymbol{\nabla})\, \boldsymbol{V}' - 2\boldsymbol{\Omega} \times \boldsymbol{V}' - \boldsymbol{\Omega} \times (\boldsymbol{\Omega} \times \boldsymbol{R}) + \frac{\boldsymbol{F}}{\rho} - \frac{1}{\rho}\boldsymbol{\nabla} p + \nu \nabla^2 \boldsymbol{V}'. \tag{10}$$

Equation (10) is the vector form of the Navier–Stokes equations in an aeroballistic axis system for a liquid-filled cylinder undergoing steady nutation and no linear acceleration.

In order for (10) to be solved numerically, it must be resolved into its scalar components. The individual vectors in cylindrical coordinates are

$$\boldsymbol{V}' = v_r' \hat{\boldsymbol{e}}_r + v_\phi' \hat{\boldsymbol{e}}_\phi + v_z' \hat{\boldsymbol{e}}_z, \tag{11}$$

$$\boldsymbol{R} = r\hat{\boldsymbol{e}}_r + z\hat{\boldsymbol{e}}_z, \tag{12}$$

$$\boldsymbol{\Omega} = \omega_x \cos\phi\, \hat{\boldsymbol{e}}_r - \omega_x \sin\phi\, \hat{\boldsymbol{e}}_\phi + \omega_z \hat{\boldsymbol{e}}_z, \tag{13}$$

where
$$\omega_x = -\omega_{\mathrm{N}} \sin\theta, \quad \omega_z = \omega_{\mathrm{N}} \cos\theta,$$

$\omega_{\mathrm{N}} \equiv$ nutation rate, $\theta \equiv$ nutation angle,

and
$$\boldsymbol{F} = F_r \hat{\boldsymbol{e}}_r + F_\phi \hat{\boldsymbol{e}}_\phi + F_z \hat{\boldsymbol{e}}_z. \tag{14}$$

Substituting (11)–(14) into each of the components of (10) and performing the vector operations yields the following terms:

convective acceleration

$$(\boldsymbol{V}' \cdot \boldsymbol{\nabla})\, \boldsymbol{V}' = \left(v_r' \frac{\partial v_r'}{\partial r} + \frac{v_\phi'}{r}\frac{\partial v_r'}{\partial \phi} + v_z' \frac{\partial v_r'}{\partial z} - \frac{v_\phi'^2}{r}\right)\hat{\boldsymbol{e}}_r + \left(v_r' \frac{\partial v_\phi'}{\partial r} + \frac{v_\phi'}{r}\frac{\partial v_\phi'}{\partial \phi} + v_z' \frac{\partial v_\phi'}{\partial z} + \frac{v_r' v_\phi'}{r}\right)\hat{\boldsymbol{e}}_\phi + \left(v_r' \frac{\partial v_z'}{\partial r} + \frac{v_\phi'}{r}\frac{\partial v_z'}{\partial \phi} + v_z' \frac{\partial v_z'}{\partial z}\right)\hat{\boldsymbol{e}}_z; \tag{15}$$

Coriolis acceleration

$$2\boldsymbol{\Omega} \times \boldsymbol{V}' = -(2v_z' \omega_x \sin\phi + 2v_\phi' \omega_z)\, \hat{\boldsymbol{e}}_r + (2v_r' \omega_z - 2v_z' \omega_x \cos\phi)\, \hat{\boldsymbol{e}}_\phi + (2v_\phi' \omega_x \cos\phi + 2v_r' \omega_x \sin\phi)\, \hat{\boldsymbol{e}}_z; \tag{16}$$

centrifugal acceleration

$$\boldsymbol{\Omega} \times (\boldsymbol{\Omega} \times \boldsymbol{R}') = (-r\omega_x^2 \sin^2\phi - r\omega_z^2 + z\omega_x \omega_z \cos\phi)\, \hat{\boldsymbol{e}}_r + (-z\omega_x \omega_z \sin\phi - r\omega_x^2 \sin\phi \cos\phi)\, \hat{\boldsymbol{e}}_\phi + (r\omega_x \omega_z \cos\phi - z\omega_x^2)\, \hat{\boldsymbol{e}}_z; \tag{17}$$

the body force due to gravity was found to be insignificant for the angular accelerations investigated and was ignored;

pressure force

$$\frac{1}{\rho}\boldsymbol{\nabla} p = \frac{1}{\rho}\frac{\partial p}{\partial r}\hat{\boldsymbol{e}}_r + \frac{1}{\rho r}\frac{\partial p}{\partial \phi}\hat{\boldsymbol{e}}_\phi + \frac{1}{\rho}\frac{\partial p}{\partial z}\hat{\boldsymbol{e}}_z; \tag{18}$$

viscous force

$$\nu\nabla^2 V' = \nu\left(\frac{\partial^2 v_r'}{\partial r^2}+\frac{1}{r}\frac{\partial v_r'}{\partial r}-\frac{v_r'}{r^2}+\frac{1}{r^2}\frac{\partial^2 v_r'}{\partial\phi^2}-\frac{2}{r^2}\frac{\partial v_\phi'}{\partial\phi}+\frac{\partial^2 v_r'}{\partial z^2}\right)\hat{e}_r$$
$$+\nu\left(\frac{\partial^2 v_\phi'}{\partial r^2}+\frac{1}{r}\frac{\partial v_\phi'}{\partial r}-\frac{v_\phi'}{r^2}+\frac{1}{r^2}\frac{\partial^2 v_\phi'}{\partial\phi^2}+\frac{2}{r^2}\frac{\partial v_r'}{\partial\phi}+\frac{\partial^2 v_\phi'}{\partial z^2}\right)\hat{e}_\phi$$
$$+\nu\left(\frac{\partial^2 v_z'}{\partial r^2}+\frac{1}{r}\frac{\partial v_z'}{\partial r}+\frac{1}{r^2}\frac{\partial^2 v_z'}{\partial\phi^2}+\frac{\partial^2 v_z'}{\partial z^2}\right)\hat{e}_z. \tag{19}$$

All of these terms can be collected to form the three scalar Navier–Stokes equations.

The remaining fluid-flow equation is the continuity equation

$$\nabla\cdot V = 0.$$

Substituting (2) and performing the vector operations yields

$$\frac{\partial v_r'}{\partial r}+\frac{v_r'}{r}+\frac{1}{r}\frac{\partial v_\phi'}{\partial\phi}+\frac{\partial v_z'}{\partial z}=0. \tag{20}$$

The axis rotation has no effect on the continuity equation.

2.3. *Boundary conditions*

The imposed boundary conditions are that the fluid adheres to the wall and that there is no flow through the wall. Therefore the conditions to be met at the cylinder and endwalls are

$$v_r'=0, \quad v_\phi'=r\omega_s, \quad v_z'=0, \tag{21}$$

where ω_s is the spin rate relative to the aeroballistic axes. The boundary condition on v_ϕ' occurs because the cylinder is spinning relative to the coordinate axes.

For highly viscous fluids the fluid motion will be dominated by the solid body rotation of the fluid, i.e. $v_\phi' \approx r\omega_s$. In order to more easily understand the deviation of the fluid motion from solid-body rotation, it is convenient to eliminate the solid-body rotation of the flow field. This may be accomplished by making the velocity reference transformation

$$v_r'=v_r, \quad v_\phi'=v_\phi+r\omega_s, \quad v_z'=v_z. \tag{22}$$

Substituting these definitions into the scalar form of the Navier–Stokes equations and letting

$$\omega_p=\omega_s+\omega_z$$

one has

$$\frac{\partial v_r}{\partial t}=-v_r\frac{\partial v_r}{\partial r}-\frac{v_\phi}{r}\frac{\partial v_r}{\partial\phi}-v_z\frac{\partial v_r}{\partial z}+\frac{v_\phi^2}{r}-\omega_s\frac{\partial v_r}{\partial\phi}+2v_\phi\omega_p$$
$$+2v_z\omega_x\sin\phi+r\omega_p^2+r\omega_x^2\sin^2\phi-z\omega_x\omega_z\cos\phi$$
$$-\frac{1}{\rho}\frac{\partial p}{\partial r}+\nu\left(\frac{\partial^2 v_r}{\partial r^2}+\frac{1}{r}\frac{\partial v_r}{\partial r}-\frac{v_r}{r^2}+\frac{1}{r^2}\frac{\partial^2 v_r}{\partial\phi^2}-\frac{2}{r^2}\frac{\partial v_\phi}{\partial\phi}+\frac{\partial^2 v_r}{\partial z^2}\right), \tag{23}$$

$$\frac{\partial v_\phi}{\partial t}=-v_r\frac{\partial v_\phi}{\partial r}-\frac{v_\phi}{r}\frac{\partial v_\phi}{\partial\phi}-v_z\frac{\partial v_\phi}{\partial z}-\frac{v_r v_\phi}{r}-\omega_s\frac{\partial v_\phi}{\partial\phi}-2v_r\omega_p$$
$$+2v_z\omega_x\cos\phi+z\omega_x\omega_z\sin\phi+r\omega_x^2\sin\phi\cos\phi$$
$$-\frac{1}{\rho r}\frac{\partial p}{\partial\phi}+\nu\left(\frac{\partial^2 v_\phi}{\partial r^2}+\frac{1}{r}\frac{\partial v_\phi}{\partial r}-\frac{v_\phi}{r^2}+\frac{1}{r^2}\frac{\partial^2 v_\phi}{\partial\phi^2}+\frac{2}{r^2}\frac{\partial v_r}{\partial\phi}+\frac{\partial^2 v_\phi}{\partial z^2}\right), \tag{24}$$

$$\frac{\partial v_z}{\partial t} = -v_r\frac{\partial v_z}{\partial r} - \frac{v_\phi}{r}\frac{\partial v_z}{\partial \phi} - v_z\frac{\partial v_z}{\partial z} - \omega_s\frac{\partial v_z}{\partial \phi} - 2v_\phi\omega_x\cos\phi$$
$$-2v_r\omega_x\sin\phi - 2r\omega_s\omega_x\cos\phi - r\omega_x\omega_z\cos\phi + z\omega_x^2$$
$$-\frac{1}{\rho}\frac{\partial p}{\partial z} + \nu\left(\frac{\partial^2 v_z}{\partial r^2} + \frac{1}{r}\frac{\partial v_z}{\partial r} + \frac{1}{r^2}\frac{\partial^2 v_z}{\partial \phi^2} + \frac{\partial^2 v_z}{\partial z^2}\right). \tag{25}$$

The continuity equation becomes

$$\frac{\partial v_r}{\partial r} + \frac{v_r}{r} + \frac{1}{r}\frac{\partial v_\phi}{\partial \phi} + \frac{\partial v_z}{\partial z} = 0. \tag{26}$$

The boundary conditions at the surface are now

$$v_r = v_\phi = v_z = 0. \tag{27}$$

While these boundary conditions are identical with those for equations written in a body-fixed coordinate system, it must be understood that (23)–(26) are still written in an aeroballistic system. The transformation of the velocity reference has done nothing to change the character of these equations and their solution.

3. Computational technique

3.1. *Finite-difference method*

The three-dimensional equations of motion developed in §2 are solved for a steady-state solution by an iterative finite-difference procedure. The iterative method chosen to solve these primitive variable equations is Chorin's (1967*a*, *b*, 1968) method of artificial compressibility. This method has advantages over the other available methods (e.g. vector potential and particle-in-cell) for solving incompressible problems, in that it directly satisfies the continuity equation and the physical boundary conditions. The present work appears to be one of the few applications of this method to a three-dimensional problem, and, to our knowledge, the first application to a non-inertial problem.

Chorin's method is based on introducing an auxiliary continuity equation

$$\frac{\partial \rho}{\partial t} = -\rho\left[\frac{\partial v_r}{\partial r} + \frac{v_r}{r} + \frac{1}{r}\frac{\partial v_\phi}{\partial \phi} + \frac{\partial v_z}{\partial z}\right] \tag{28}$$

and an artificial equation of state

$$p = \rho/\delta \tag{29}$$

where δ is a constant to be determined.

Using the artificial equation of state, Chorin has cast the auxiliary continuity and the momentum equations in terms of either p or ρ. In this work we have chosen to use p so that the momentum equations remain unchanged, and the auxiliary continuity equation becomes

$$\frac{\partial p}{\partial t} = -\frac{\rho}{\delta}\left[\frac{\partial v_r}{\partial r} + \frac{v_r}{r} + \frac{1}{r}\frac{\partial v_\phi}{\partial \phi} + \frac{\partial v_z}{\partial z}\right]. \tag{30}$$

In this equation t serves as an iterative variable, which is analogous to time in a time-varying compressible-flow problem. δ serves as a relaxation parameter in the iterative procedure. As the solution converges, $\partial p/\partial t \to 0$, and the incompressible continuity equation is approached. In the limit, $\partial p/\partial t = 0$, and the constant factor

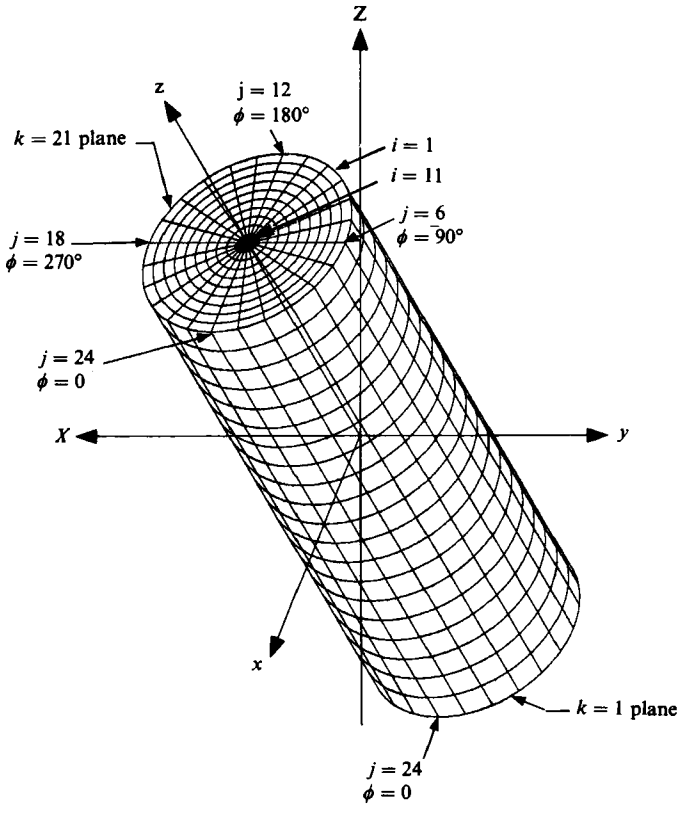

FIGURE 2. Grid system.

δ disappears. In a numerical method, convergence is stated as $\Delta p/\Delta t < \epsilon$, where ϵ is an arbitrary convergence criterion. Therefore it is seen that δ is absorbed by the convergence criterion ϵ and does not affect the converged solution.

The finite-difference grid system used in the present method is shown schematically in figure 2. Indices i, j and k refer to the radial, circumferential and axial coordinates respectively, such that

$$\left.\begin{aligned} r &= R-(i-1)\,\Delta r \quad (i = 1,2,\ldots,N),\\ \phi &= j\,\Delta\phi \qquad\qquad (j = 1,2,\ldots,M),\\ z &= \tfrac{1}{2}(k-1)\,\Delta z l \quad (k = 1,2,\ldots,L) \end{aligned}\right\} \tag{31}$$

R is the radius of the cylinder and l is the length of the cylinder. In the present calculations N, M and L were chosen to be 11, 24 and 21 respectively, yielding 5544 grids points. This grid density gave good resolution and moderate computational time on the Cray-1S computer.

The finite-difference approximations applied to the Navier–Stokes equations (23)–(25) and to the auxiliary continuity equation (30) are forward-time centred-space differences. They are first-order accurate in time and second order in all spatial directions. The first-order accuracy of the time differences does not enter into the global accuracy of the solution because only steady-state solutions are of interest. As a result, the numerical approximations to the converged governing equations are second-order accurate.

3.2. *Initial and boundary conditions*

The initial conditions of the fluid do not affect the converged solution of the flow field, but they are important in reducing the number of iterations required for convergence. The initial state chosen is solid-body rotation of the fluid. The initial conditions on the velocity components, shifted according to (22), are

$$v_r = v_\phi = v_z = 0. \tag{32}$$

The initial conditions on the pressure field are obtained by setting all terms involving fluid velocity and all Coriolis terms to zero in the momentum equations. From (23)–(25) one obtains

$$\frac{\partial p}{\partial r} = \rho(r\omega_{\mathrm{p}}^2 + r\omega_x^2 \sin^2\phi - z\omega_x\omega_z\cos\phi), \tag{33}$$

$$\frac{1}{r}\frac{\partial p}{\partial \phi} = \rho(r\omega_x^2 \sin\phi\cos\phi + z\omega_x\omega_z\sin\phi), \tag{34}$$

$$\frac{\partial p}{\partial z} = \rho(-r\omega_x\omega_z\cos\phi + z\omega_x^2). \tag{35}$$

Integrating these results in an expression for pressure

$$p = \rho(\tfrac{1}{2}r^2\omega_{\mathrm{p}}^2 - rz\omega_x\omega_z\cos\phi + \tfrac{1}{2}r^2\omega_x^2\sin^2\phi + \tfrac{1}{2}z^2\omega_x^2) + p_0. \tag{36}$$

The constant of integration p_0 is the initial static pressure in the non-spinning container. In this work this value was arbitrarily set to zero.

The finite-difference form of the boundary conditions on velocity are identical with those (27) given for the continuum.

The boundary conditions on pressure are implemented directly through the auxiliary continuity equation (30).

The pressure boundary condition on the cylinder wall is

$$\left.\frac{\partial p}{\partial t}\right|_{\mathrm{w}} = -\frac{\rho}{\delta}\left.\frac{\partial v_r}{\partial r}\right|_{\mathrm{w}}, \tag{37}$$

and on the ends of the cylinder

$$\left.\frac{\partial p}{\partial t}\right|_{\mathrm{w}} = -\frac{\rho}{\delta}\left.\frac{\partial v_z}{\partial z}\right|_{\mathrm{w}}. \tag{38}$$

Forward time differences and second-order one-sided spatial differences were used for (37) and (38). Second-order accurate boundary conditions on pressure improved the accuracy of the results compared with first-order accurate boundary conditions used earlier by Vaughn, Oberkampf & Wolfe (1983).

A special approach is required at the centre of the cylinder because the terms involving $1/r$ in the momentum and continuity equations become indeterminate. Several methods of handling the centre indeterminacy were tried, including the substitution of rectangular coordinates at the centre. Local rectangular coordinates eliminated the indeterminacy, but did not noticeably change the results compared with the following procedure. First, the calculations are started at the outside of the cylinder ($i = 1$) and proceed inward to $i = N-1$, were N is at the centre ($N = 11$). The pressures and velocities v_r and v_z are computed at the centre using a second-order

difference equation along the ray across the centre from the previously computed points. The equations are

$$v_{rN,j,k} = v_{rN-1,j,k} - \tfrac{1}{3}(v_{rN-2,j,k} + v_{rN-1,j+\frac{1}{2}M,k}), \tag{39}$$

$$v_{zN,j,k} = v_{zN-1,j,k} - \tfrac{1}{3}(v_{zN-2,j,k} - v_{zN-1,j+\frac{1}{2}M,k}), \tag{40}$$

$$p_{N,j,k} = p_{N-1,j,k} - \tfrac{1}{3}(p_{N-2,j,k} - p_{N-1,j+\frac{1}{2}M,k}). \tag{41}$$

$\frac{1}{2}M$ corresponds to a ray displaced by 180°. The velocities and pressure calculated at the centre for each circumferential ray are then averaged to obtain a final single value at the centre for a given iteration step. The circumferential velocity v_ϕ must be equal to the radial velocity at the centre on a ray displaced by 90°.

Details on the numerical procedure and iterative convergence characteristics can be found in Vaughn *et al.* (1983).

4. Discussion of results

4.1. *Nature of fluid motion*

One of the most interesting and useful results of a numerical calculation is the determination of the details of the flow. An enormous quantity of velocity-vector data is produced by a single converged solution; however, only a few velocity-vector plots will be presented which demonstrate the basic motion of the fluid. The fluid-velocity vectors shown in the figures are in the aeroballistic reference frame, and the solid-body rotation component has been eliminated, i.e. the velocity vectors shown are only the deviations from solid-body rotation. Figure 3 shows a side view of the cylinder perpendicular to a plane containing both the spin axis and the nutation axis. Figure 4 shows a side view of the cylinder parallel to a plane containing the spin and nutation axes. The view in figure 4 is perpendicular to the cylinder axis such that the z-axis is in the foreground and the Z-axis is in the background. This calculation was made for the conditions of $\theta = 20°$, $\omega_s = 3000$ r.p.m., $\omega_N = 500$ r.p.m., $\nu = 9500$ cSt, a cylinder radius of 2.375 in., and a length of 20.85 in. The motion at higher viscosities is similar, except that the velocities are not as large. Notice that there is a pronounced vortex in each end of the cylinder and a much weaker central vortex. There is also a separate outer vortex motion near the walls that rotates in the same direction as the two end vortices. This general behaviour is shown schematically in figure 5. The reader is reminded that these velocity vectors are the deviations from solid-body rotation. A single fluid particle actually moves back and forth axially in an oscillatory motion as the particle moves circumferentially at a speed near the spin rate. Consequently, the motion only appears to be a vortex in a velocity-reference-shifted aeroballistic system.

Figure 6 shows velocity-vector plots near the top ($k = 19$) and bottom ($k = 3$) ends of the cylinder, and it can be seen that the two flow patterns are similar but reversed in direction. The largest velocities in the fluid (in the velocity-shifted frame) occur near the endwalls. It is here that the axial vortex motion is reversed from opposite sides of the cylinder and turned parallel to the endwalls.

Figure 7 is a polar vector plot at the centre axial station ($k = 11$). This clearly shows that there is a slow rotation of the fluid about the spin axis, relative to the aeroballistic axis, in a direction opposite to the spin direction. This produces a viscous shear and a roll torque opposite to the counterclockwise spin direction.

Figure 8 is a map of the cylinder wall as viewed from the inside, showing the circumferential component of wall shear-stress vectors. These circumferential wall

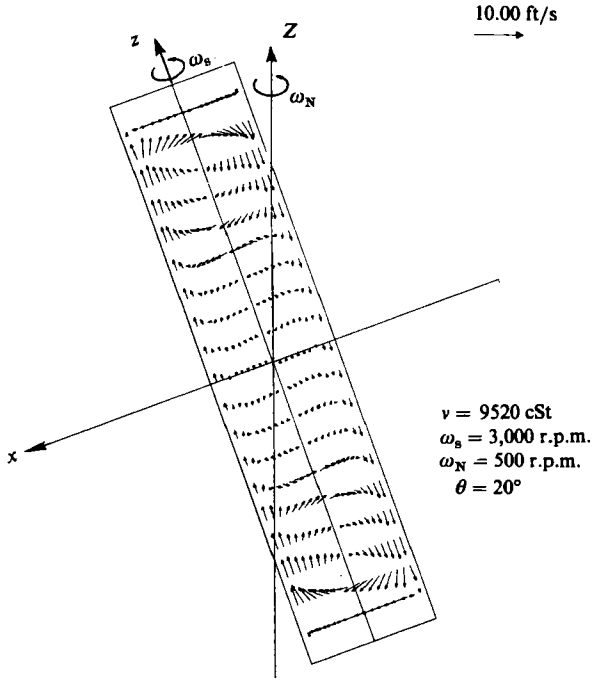

FIGURE 3. Fluid velocity-vector plot (side view perpendicular to (z, Z)-plane).

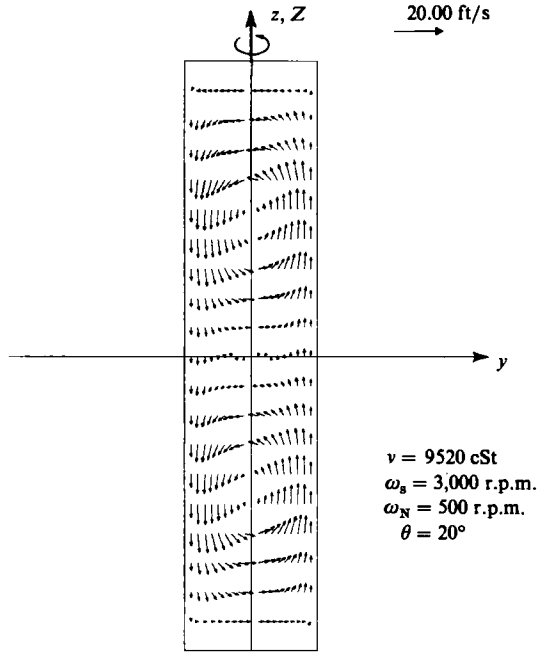

FIGURE 4. Fluid velocity-vector plot (side view through plane of nutation angle).

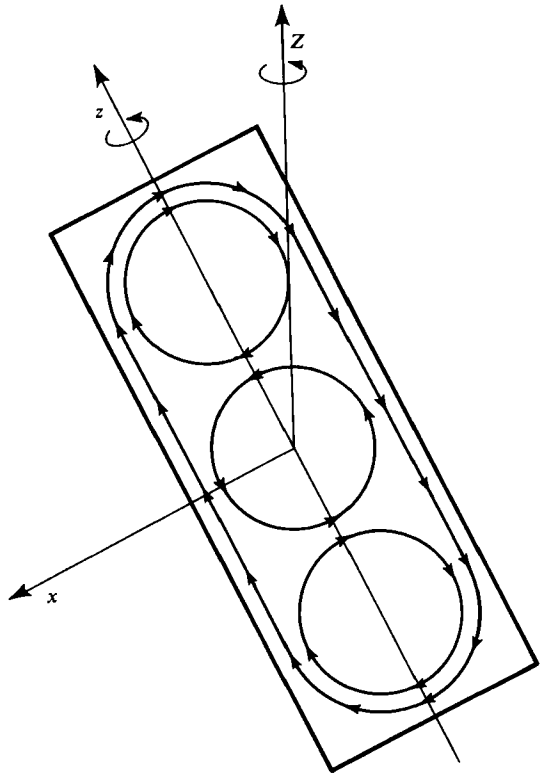

FIGURE 5. Schematic of the fluid flow.

shear-stress vectors are proportional to the velocity component v_ϕ adjacent to the wall. When viewed in this manner, the cylinder wall would be moving upward as a result of spin. It can be seen that circumferential velocity components are predominantly downward in the opposite direction, resulting in the shear forces on the wall that produce the despin torque. The despin moment can only be produced by the viscous shear forces because a force generated by pressure cannot have a tangential component. Note that only one-half the grid points are shown in the circumferential direction in the interest of clarity.

The plane of maximal axial and transverse velocity is canted with respect to the plane of the nutation angle by roughly 45°, which results in producing both a pitch and yaw moment. The pitch and yaw moments are produced by both viscous shear forces and pressure forces. As an example of the relative contribution of each of the components to the total liquid induced pitch and yaw moment, consider the following case: $\nu = 80000$ cSt, $\omega_S = 3000$ r.p.m., $\omega_N = 500$ r.p.m., $\theta = 20°$, cylinder radius of 2.180 in., and length of 19.617 in. The integrated values of the moments for this case are as follows.

Pitch moment:

viscous component = −22.9 ft lb (−20.1 on cylinder, −2.8 on ends);
pressure component = +64.5 ft lb (72.4 on cylinder, −7.9 on ends);
net liquid moment = +41.6 ft lb.

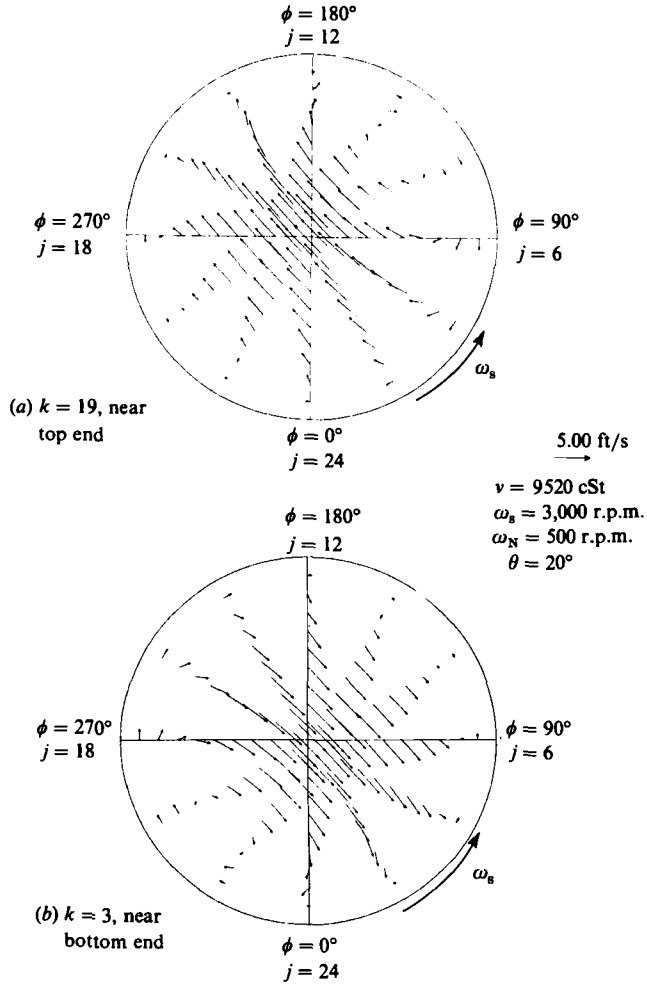

FIGURE 6. Fluid-velocity vector plot (cross-section near ends).

Yaw moment:

viscous component = +12.69 ft lb (+11.70 on cylinder, +0.99 on ends);
pressure component = −17.01 ft lb (−18.55 on cylinder, +1.54 on ends);
net liquid moment = −4.32 ft lb.

It can be seen that while the pressure component is larger for each moment, the viscous component is significant. For each component in both pitch and yaw the liquid moment on the sides of the cylinder dominates that produced on the ends of the cylinder. For the liquid-induced yaw moment it is seen that the net yaw moment is a near balance between countervailing forces of viscosity and pressure. A simple calculation shows that if the liquid acted as a solid body the pitch moment would be 30.5 ft lb and the yaw moment would be zero. This indicates that, for the case given here, the effect of the fluid fill is destabilizing in both pitch and yaw.

The numerical results show very clearly that the motion of a fluid particle is predominantly oscillatory in nature, and is combined with a slow circumferential drift relative to the cylinder wall. The frequency of oscillation of a fluid particle is near the spin rate, and the amplitude of the motion is very small. This may explain why

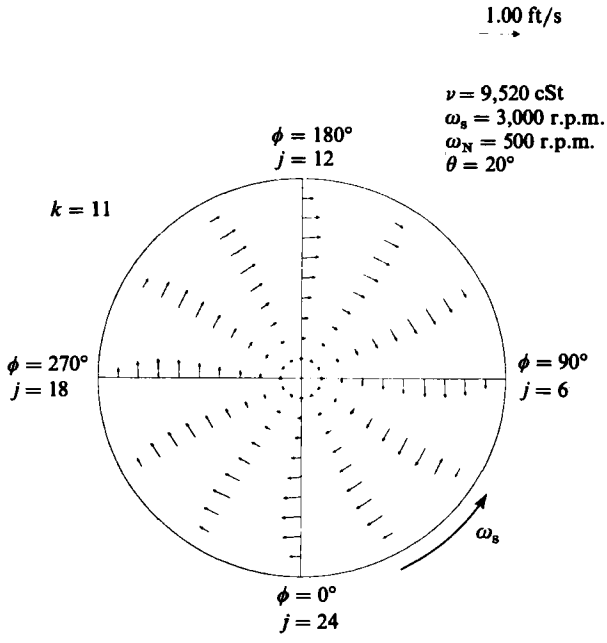

FIGURE 7. Fluid-velocity vector plot (cross-section at centre of cylinder).

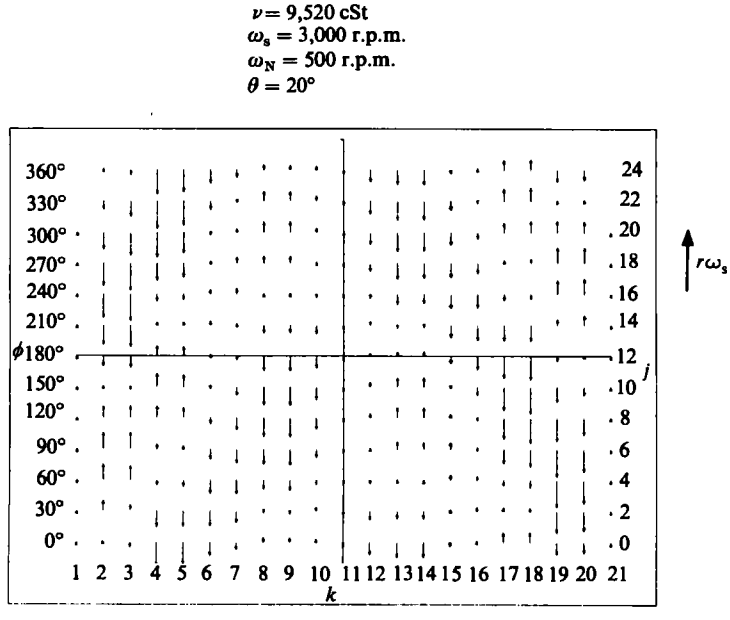

FIGURE 8. Circumferential wall shear-stress vectors.

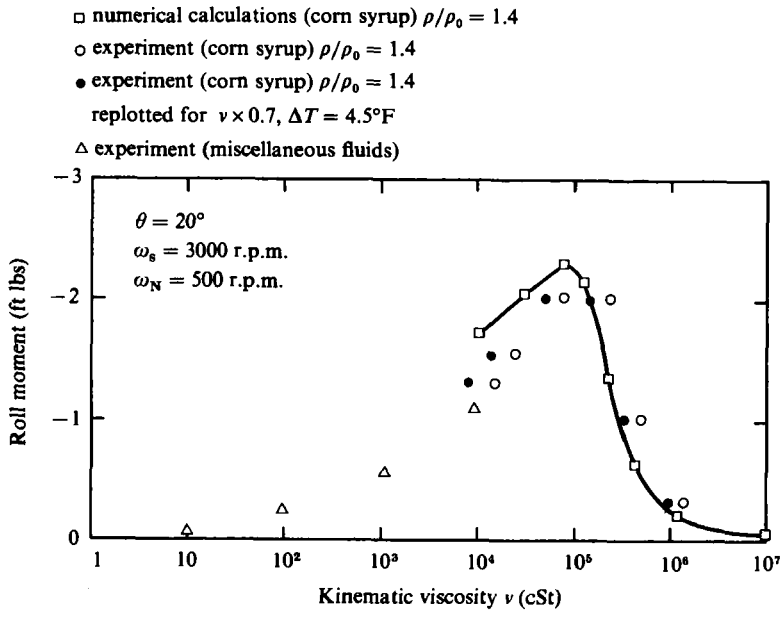

FIGURE 9. Comparison of calculated and experimental roll moment at various viscosities (experiment, Miller 1982).

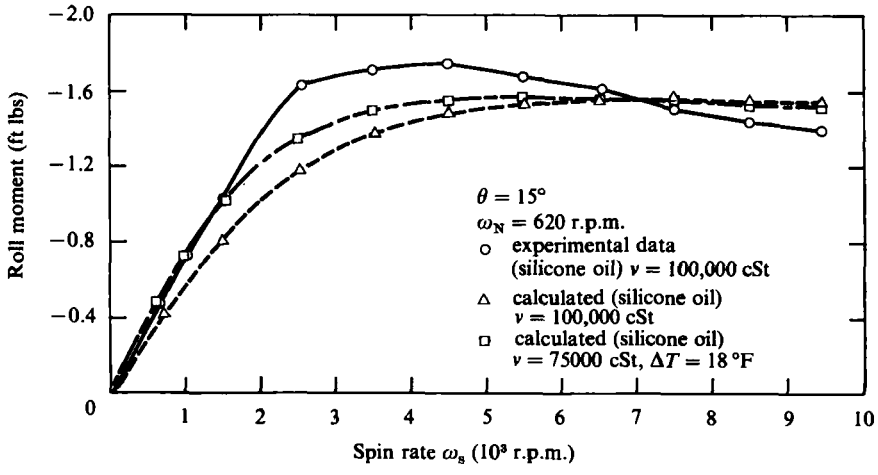

FIGURE 10. Comparison of calculated and experimental roll moment at various spin rates (experiment, Miller 1982).

large cell baffles have been ineffective and why small-cell porous fillers, such as felt, have been effective in reducing the liquid-induced moments.

In experimenting with the numerical code it was found that Coriolis accelerations appearing in the momentum equations are primarily responsible for driving the fluid motion, although the terms

$$\omega_s \frac{\partial v_r}{\partial \phi}, \quad \omega_s \frac{\partial v_\phi}{\partial \phi}, \quad \omega_s \frac{\partial v_z}{\partial \phi}$$

appearing in the three momentum equations do have a significant effect. These are the convective acceleration terms due to the cylinder spin rate ω_s.

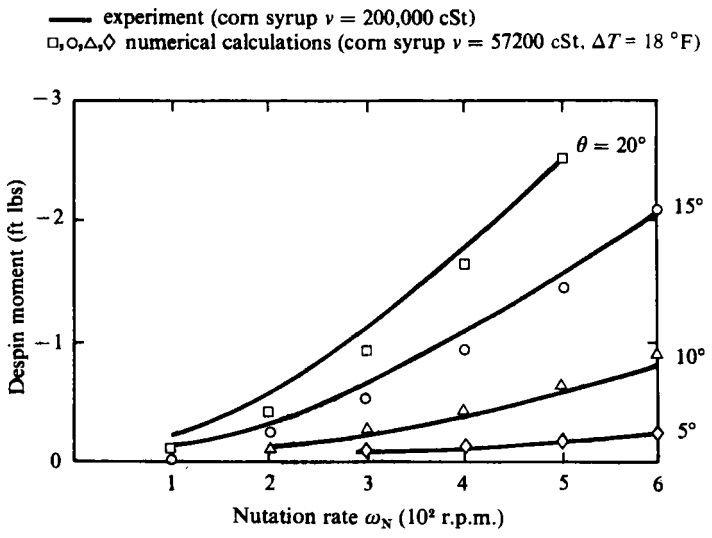

FIGURE 11. Comparison of calculated and experimental roll moment for various nutation angles and rates (experiment, Miller 1982).

4.2. *Roll moment*

Roll moment has been calculated for a cylinder with a radius of 2.375 in. and a length of 20.75 in. In attempting to compare fluid-induced moments with experimental data it became apparent that a consistent bias existed in the comparisons. Recent experimental measurements by Miller (1983 personal communication) have determined that the temperature of the fluid in the cylinder rises not only after repeated test runs, but also during a run. The temperature data indicated that the temperature increased by about 4.5 °F per run for silicon oil and roughly stabilized after repeated running at an increase of 18 °F. Consequently, the true temperature must be higher than the initial temperature and the true viscosity must be lower than the viscosity quoted for the experimental runs. Faced with this dilemma, we have tried to make a viscosity correction for each type of data run.

The first comparison (figure 9) shows computed and experimental data for despin moment versus viscosity. In this case, each experimental data point resulted from a single run, where the initial temperature was adjusted before each run to obtain the correct initial viscosity. Consequently, according to the subsequent temperature data, one would expect a temperature increase of roughly 4.5 °F for each point. The experimental data points have been shown both uncorrected (○) and corrected (●) for a 4.5 °F temperature increase. It can be seen that the calculated values are in fair agreement with the corrected data.

In the comparison of the experimental data for despin moment at various spin rates, calculations were made for two viscosities (figure 10), $\nu = 100000$ cSt and 75000 cSt, the latter corresponding to an 18 °F temperature increase. In this case, the data were taken in a more continuous process so that a temperature increase near the experimentally observed maximum should be expected. Again, the experimental data are predicted reasonably well by the numerical solution.

In figure 11 the calculated despin moment is shown as a function of nutation angle and rate. In this case, we have chosen to make the calculations at a viscosity of 57200 cSt, which is equivalent to an 18 °F correction from the initial viscosity of

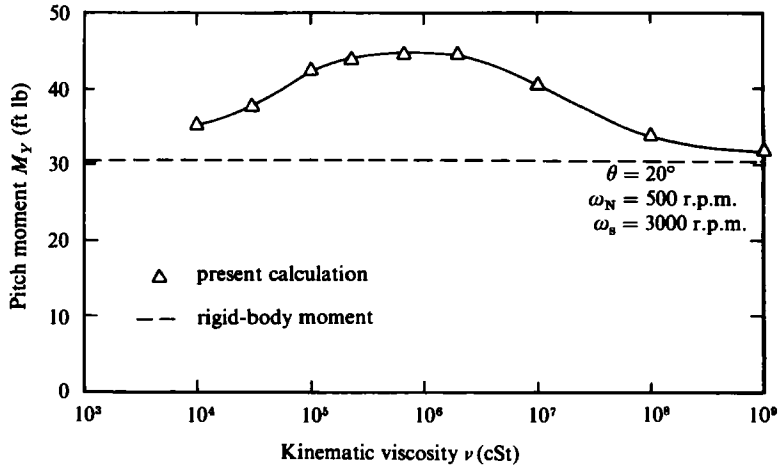

FIGURE 12. Calculated pitch moment *vs.* viscosity.

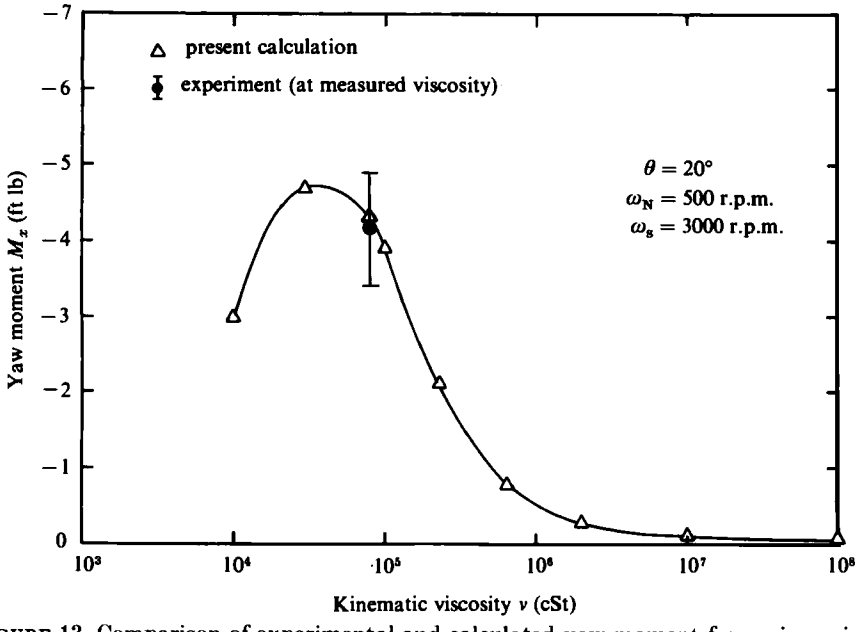

FIGURE 13. Comparison of experimental and calculated yaw moment for various viscosities (experiment, Miller 1983, personal communication).

200000 cSt and is the maximum steady-state temperature increase observed in the recent temperature increase tests. It should be observed that the calculated roll moment does not change radically over this viscosity range, as can be seen in figure 9. Again, the numerical procedure predicts the experimental data reasonably well.

4.3. *Pitch moment*

Pitch and yaw moments have been calculated for a cylinder with a radius of 2.180 in. and a length of 19.617 in. The calculated pitch moment as a function of viscosity is shown in figure 12 for silicone oil. Comparison is made with the rigid-body pitch moment because there are no existing laboratory experimental measurements for comparison. It can be seen that as the viscosity increases, the pitch moment

approaches that of the rigid body. This is the proper trend, because a rigid body is equivalent to a fluid body with infinite viscosity. It should be noticed that the effect of the fluid is to slightly decrease the projectile stability in pitch, i.e. the fluid motion causes a larger positive (destabilizing) moment than that of an equivalent rigid body.

4.4. *Yaw moment*

The calculated values of yaw moment as a function of viscosity for silicone oil are shown in figure 13. It can be seen that the variation of the yaw moment is similar to the calculated roll moment as seen in figure 9. The prediction is in excellent agreement with the experimental measurement at 80 000 cSt. The single experimental measurement (Miller 1983 personal communication) was recently obtained by a newly developed experimental technique. As discussed earlier, the liquid-induced yaw moment is a near balance of the positive moment produced by the wall shear stress and the negative moment produced by the normal stress. The net liquid-induced yaw moment (negative) acts in the direction to increase the nutation rate which is destabilizing in the flight of a projectile and would result in a growth of the nutation angle. This has been observed in free flight of liquid filled projectiles (D'Amico 1978; D'Amico & Miller 1979; Miller 1982).

5. Concluding remarks

The three-dimensional incompressible Navier–Stokes equations are solved numerically for a fluid-filled cylindrical canister that is spinning and nutating. The results show that the motion of the fluid is steady relative to the aeroballistic axis system. This means, consequently, that the flow field is time-varying, i.e. periodic, in a body-fixed system. There is no evidence of pressure waves or resonance phenomena for the range of viscosities examined, 0.9×10^4–1.0×10^9 cSt. The internal fluid motion appears to be driven primarily by the Coriolis-acceleration terms in the momentum equations. The general motion of fluid particles is a nearly circular orbit whose plane is tilted to the cylinder spin axis. There is a slow continuous circumferential drift of the fluid particles opposite to the direction of the spin rate. This accounts for the despin moment through viscous shear interaction with the cylinder wall.

The results of the numerical calculations agree reasonably well with existing experimental results, provided that corrections are made for the reduction in viscosity that results from heating during the experimental test. The roll and yaw moments reach a maximum at a kinematic viscosity of approximately 80 000 cSt. The roll moment results entirely from viscous shear forces, while the pitch and yaw moments result from both viscous shear and pressure forces.

The despin moment is roughly proportional to the square of the nutation angle and the square of the nutation rate. It also is approximately proportional to the density of the fluid. There does not appear to be any simple dependency between the despin moment and the spin rate or viscosity. For a given coning angle and rate, the despin moment increases with spin rate until a threshhold value and then remains constant with spin rate. This result shows good agreement with experimental data.

For the particular cases investigated, it was found that the liquid-induced pitch moment was slightly larger than the rigid-body value. For extremely high viscosities, e.g. 10^9 cSt, the liquid pitch moment is nearly equal to the rigid-body value. The liquid-induced yaw moment varies with spin rate in a fashion very similar to the despin moment. The yaw-moment prediction is in excellent agreement with the only available experimental measurement. The yaw moment is a near balance of the

positive moment produced by the wall shear stress and the negative moment produced by the normal stress.

The present numerical solutions are limited to fluids with viscosities of 9000 cSt and greater, at least for this cylindrical configuration and at the spin and nutation conditions used in the calculations. Other conditions may allow stable solutions to be obtained at lower viscosities. The present numerical method converges in about four minutes for the higher viscosity fluids on the CRAY-1S computer, and therefore provides a practical computational method. The reason for non-convergent solutions at viscosities below 9000 cSt is not clear. It could be speculated that there is some shortcoming in the numerical method for low viscosities, or it could be that no steady state solution in the aeroballistic frame exists for low viscosities.

This work was done at Sandia National Laboratories. It was supported by the U.S. Department of Energy under Contract DE-AC04-76DP00789 and by the Chemical Research and Development Center, United States Army Armament, Munitions, and Chemical Command, under Military Interdepartmental Purchase Request 3311-1409.

REFERENCES

CHORIN, A. J. 1967*a* *J. Comp. Phys.* **2**, 12–26.

CHORIN, A. J. 1967*b* *Am. Math. Soc. Bull.* **73**, 928–931.

CHORIN, A. J. 1968 *Math. Comp.* **22**, 745–762.

D'AMICO, W. P. 1978 *US Army Ballistics Res. Lab. Memo. Rep.* 02806.

D'AMICO, W. P. 1981 *US Army Ballistics Res. Lab. Memo. Rep.* 03072.

D'AMICO, W. P. & MILLER, M. C. 1979 *J. Spacecraft & Rockets* **16**, 62–64.

MERIAM, J. L. 1975 *Dynamics*, 2nd edn. Wiley.

MILLER, M. C. 1979 *US Army Chem. Syst. Lab. Special Publication* 79005.

MILLER, M. C. 1981 *J. Spacecraft & Rockets* **18**, 286–288.

MILLER, M. C. 1982 *J. Guidance & Control* **5**, 151–157.

MURPHY, C. H. 1982 *US Army Ballistics Res. Lab. Memo. Rep.* 03194.

MURPHY, C. H. 1983 *US Army Ballistics Res. Lab. Tech. Rep.* 2521.

RAUDKIVI, A. J. & CALLANDER, R. A. 1975 *Advanced Fluid Mechanics.* Wiley.

SCHLICHTING, H. 1968 *Boundary Layer Theory*, 6th edn. McGraw-Hill.

STEWARTSON, K. 1969 *J. Fluid Mech.* **5**, 577–592.

VAUGHN, H. R. 1978 *Sandia Natl Labs Rep.* SAND78-0999.

VAUGHN, H. R., OBERKAMPF, W. L. & WOLFE, W. P. 1983 *Sandia Natl Labs Rep.* SAND83-1789.

WEDEMEYER, E. H. 1966 *US Army Ballistics Res. Lab. Rep.* 1325.